ChemComm

COMMUNICATION

View Article Online
View Journal | View Issue

Cite this: *Chem. Commun.*, 2024, **60**, 14073

Received 23rd July 2024,
Accepted 5th November 2024

DOI: 10.1039/d4cc03701d

rsc.li/chemcomm

Tunable synthesis of magnetoelectric $CoFe_2O_4$–$BaTiO_3$ core–shell nanowires†

Noah D. Ferson,[a] John R. Ganiban,[a] David P. Arnold[b] and Jennifer S. Andrew *[a]

A template-assisted synthesis approach was employed to tune the structure and properties of $CoFe_2O_4$–$BaTiO_3$ core–shell magnetoelectric nanowires. By adjusting the composition of the nanowires, we achieved control over the magnetic anisotropy in the $CoFe_2O_4$ core phase. This work highlights the potential for enhanced magnetic anisotropy to improve magnetoelectric performance.

Multiferroics are a class of multifunctional materials that combine at least two ferroic ordering parameters, *e.g.*, ferroelectric, ferromagnetic, and ferroelastic. The ferroic orderings, along with their respective properties of polarization, magnetization, and strain, are well suited for use in collective state switches, resulting in significant interest in multiferroics for novel memory and logic devices.[1–4] In these applications, device scalability is crucial for continued enhancements in memory and compute density. Nanostructured multiferroics offer particular advantages in these applications, where, compared to their bulk counterparts, they are expected to exhibit enhanced magnetoelectric coupling coefficients and demonstrate superior scalability.[1,5–8]

A key property of multiferroic materials is their magnetoelectric (ME) coupling, which enables the voltage control of magnetism, and *vice versa*. Composite ME materials, where a piezoelectric is strain-coupled with a magnetostrictive material, overcome limitations attributed to single-phase ME multiferroics (*e.g.*, ordering temperatures well below room temperature).[9] In a nanostructured ME composite, the interfacial area between the magnetostrictive and piezoelectric phases is maximized, facilitating greater strain transfer and enhanced coupling.[9] Moreover, high aspect ratio nanostructures, such as nanowires, offer a method to investigate the effects of anisotropy on the resulting ME properties.[7,10,11] In this work, we specifically investigate the contribution of magnetic anisotropy and its tunability by controlling the relative fractions of the core and shell phases in magnetoelectric $CoFe_2O_4$–$BaTiO_3$ core–shell nanowires.

Core–shell nanowires have previously been fabricated using several techniques, including coaxial electrospinning,[12,13] template-assisted methods,[14] and solvo-/hydro- thermal processes.[15,16] Among these, template-assisted approaches are particularly promising and can be applied in conjunction with sol–gel processing and electrochemical techniques for the fabrication of high quality nanocomposites with tailored compositions. While core–shell magnetoelectric nanowires have been previously synthesized using template-assisted methods,[14,17] the effect of varying the fraction of the core and shell phases on their properties has rarely been studied. Here, we demonstrate that compositional variance in magnetoelectric $CoFe_2O_4$–$BaTiO_3$ nanowires can be varied using synthetic procedures to generate ME nanowires with tunable magnetic anisotropy and ME coupling.

Magnetoelectric core–shell nanowires were fabricated in an anodic aluminum oxide (AAO) template, where $BaTiO_3$ shells were first fabricated, followed by electrodeposition and oxidation of $CoFe_2$ to form $CoFe_2O_4$–$BaTiO_3$ core–shell nanowires. An overview of the process is presented in Fig. 1a (a complete description of the core–shell nanowire synthesis and characterization is included within the ESI†). Briefly, AAO templates were coated with an amorphous $BaTiO_3$ gel *via* a vacuum-assisted sol–gel template wetting process. The thickness of the $BaTiO_3$ gel can be increased by repeating the template wetting process multiple times. The amorphous $BaTiO_3$ gel was then crystallized by calcination at 650 °C for 6 hours. Fig. 1b shows that the $BaTiO_3$ yield increases and then plateaus after three wetting cycles, demonstrating the ability to tune $BaTiO_3$ yield *via* increasing the number of wetting cycles. The plateau in yield for samples prepared with more than three wetting cycles is attributed to the decreasing sol–gel stability, as the solution continues to undergo hydrolysis and condensation reactions due to the extended time required for template wetting. This

[a] *Dept. of Materials Science & Engineering, University of Florida, Gainesville, FL 32611, USA. E-mail: jandrew@mse.ufl.edu*
[b] *Dept. of Electrical & Computer Engineering, University of Florida, Gainesville, FL 32611, USA*

† Electronic supplementary information (ESI) available. See DOI: https://doi.org/10.1039/d4cc03701d

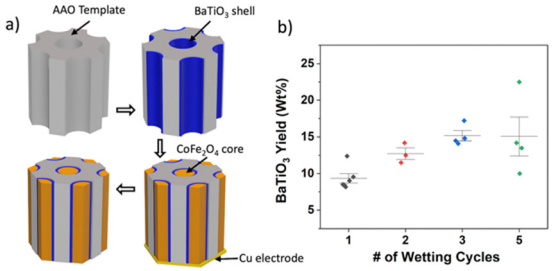

Fig. 1 (a) Schematic of porous anodic aluminium oxide (AAO) template based $CoFe_2O_4$–$BaTiO_3$ core–shell nanowire synthesis with open arrows indicating synthesis path and (b) $BaTiO_3$ nanotube yield in AAO templates after calcination with respect to the number of wetting cycles used during synthesis.

limitation could potentially be addressed by developing a more stable $BaTiO_3$ sol–gel solution, possibly by the addition of chelating agents.

To complete the core–shell nanowire synthesis, a $CoFe_2$ core was deposited *via* electrochemical deposition into the $BaTiO_3$ shells. The final schematic in Fig. 1a depicts the core–shell nanowires within the AAO template. To generate free-standing nanowires, the AAO template can be preferentially etched using 2 M NaOH to facilitate nanowire release.

X-ray diffractometry (XRD) was performed on free-standing nanowires to confirm the formation of perovskite $BaTiO_3$ and spinel $CoFe_2O_4$ (Fig. S1, ESI†). Peaks characteristic of tetragonal $BaTiO_3$ were indexed from the diffraction patterns. However, peak splitting arising from the elongated *c*-axis in the perovskite structure cannot be distinguished due to the nanocrystalline nature of the $BaTiO_3$ nanotubes.[18] Consequently, additional phase identification was performed using Raman spectroscopy, which probes intermediate and long range ordering. Modes typical of tetragonal perovskite $BaTiO_3$ are revealed in Fig. S2 (ESI†). For example, the band at *ca.* 307 cm^{-1} is attributed to the B_1 and E(TO + LO) phonon modes, which are characteristic to the polar tetragonal phase of $BaTiO_3$.[19,20]

The nanowire morphology was then evaluated using a combination of scanning electron microscopy (SEM), focus ion beam SEM (FIB-SEM), and scanning transmission electron microscopy (STEM). Fig. 2a shows a longitudinal cross-section of the AAO template with embedded core–shell nanowires, while Fig. 2b displays the free-standing core–shell nanowires after chemical etching of the AAO template. A transverse cross section of nanowires in template was prepared using FIB-SEM (Fig. 2c), demonstrating the complete filling of pores. The high angle annular dark field (HAADF) micrograph shown in Fig. 2d reveals the core–shell morphology with a distinct interface between the constituent phases.

Next, vibrating sample magnetometry (VSM) was performed on free-standing nanowires after release from their templates. Mass-magnetization curves are presented in Fig. 3 for samples prepared with zero to three $BaTiO_3$ wetting cycles. The fraction of $CoFe_2O_4$ in core–shell nanowires was established by comparing $CoFe_2O_4$ saturation magnetization (M_s) to that of $CoFe_2O_4$ nanowires (M_s = 16.7 emu g^{-1}) prepared with zero $BaTiO_3$ wetting cycles. Nanowires prepared with one and three wetting cycles contain 88.7, and 74.7 wt% $CoFe_2O_4$, respectively, indicating the composition of the core–shell nanowires can be tuned by increasing the number of $BaTiO_3$ template wetting cycles. The reduced M_s of the $CoFe_2O_4$ nanowires presented here, compared to the bulk value of approximately 80 emu g^{-1}, aligns with previous studies for $CoFe_2O_4$ nanowires heat treated at 600 °C.[21] This reduction has been attributed to their small average crystallite sizes (16.1 nm from Scherrer's analysis, ESI†).

Magnetoelectric coupling in core–shell nanowires was investigated by examining their magnetic properties before and after *in situ* thermal depolarization. Prior to magnetic measurements, the nanowires were electrically poled *ex situ via* corona poling (a complete description of the experimental details are included within the ESI†). Fig. 4a displays a room temperature VSM hysteresis loop for electrically poled core–shell nanowires prepared with three $BaTiO_3$ wetting cycles before (blue, dashed) and after (orange, solid) thermal depolarization. Upon examining the hysteresis loop, it was observed that the M_s increased after thermal depolarization. This indicates that the corona poling process initially decreased the M_s of the $CoFe_2O_4$ core as a remnant strain was generated within the $BaTiO_3$ shell. These results are consistent with previous work investigating magnetoelectric coupling in mesoporous ME composites.[22]

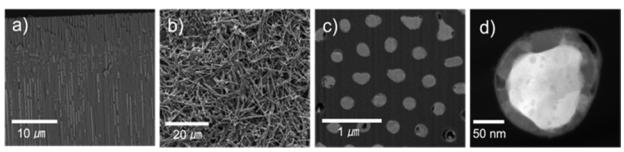

Fig. 2 (a) Longitudinal cross sectional electron micrograph of core–shell nanowires after deposition into the AAO template, (b) freestanding nanowires after release *via* chemical etching, (c) FIB transverse cross section of nanowires in AAO, and (d) STEM-HAADF image of a core–shell nanowire cross section.

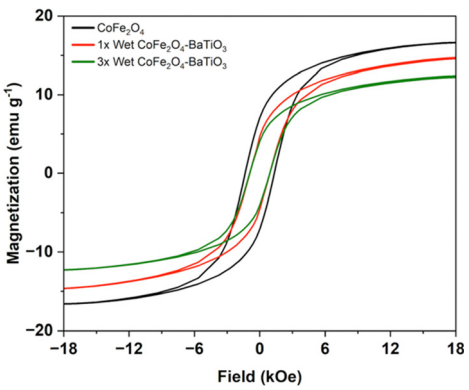

Fig. 3 VSM hysteresis loops for $CoFe_2O_4$ nanowires (black) and core–shell nanowires prepared with one (red) and three (green) $BaTiO_3$ wetting cycles.

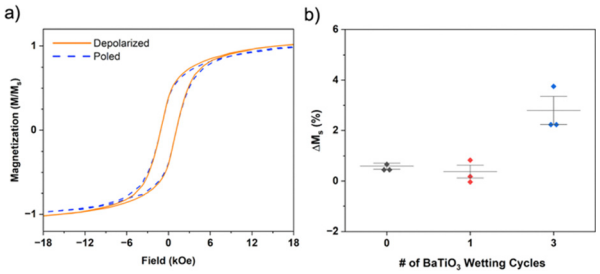

Fig. 4 (a) Magnetization *vs.* field data for *ex situ* poled nanowires *via* a corona discharge process (blue) and after *in situ* thermal depolarization (orange) and (b) compiled change in saturation magnetization (ΔM_s) with respect to the number of $BaTiO_3$ wetting cycles implemented during synthesis.

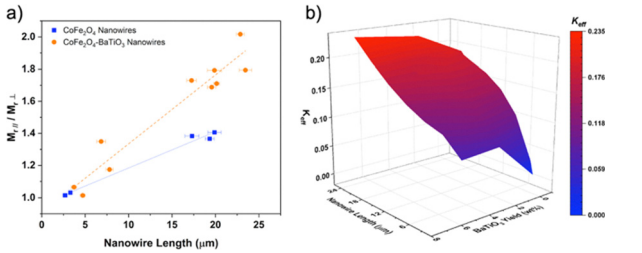

Fig. 5 (a) Magnetic texture ($M_{r\parallel}/M_{r\perp}$) as a function of nanowire length for $CoFe_2O_4$ nanowires (blue square) and core–shell nanowires (orange closed circle), error bars represent the standard deviation for the nanowire lengths. (b) Surface plot of the effective anisotropy constant (K_{eff}) for $CoFe_2O_4$–$BaTiO_3$ nanowires in template as a function of nanowire length and the recorded $BaTiO_3$ yield during synthesis.

The percent change in saturation magnetization (ΔM_s) was quantified for nanowires before (poled) and after (depoled) thermal depolarization according to eqn (1).

$$\Delta M_s = \frac{\left(M_{s_{Depoled}} - M_{s_{Poled}}\right)}{M_{s_{Poled}}} \times 100\% \quad (1)$$

In Fig. 4b, ΔM_s values are shown with respect to the number of $BaTiO_3$ wetting cycles implemented during synthesis. Samples prepared with zero (the pure $CoFe_2O_4$ control) and one $BaTiO_3$ wetting cycle exhibit a ΔM_s of 0.66 ± 0.21% and 0.37 ± 0.44%, respectively (representative hysteresis loops are presented in Fig S3, ESI†). The lack of coupling evident in the sample prepared with one $BaTiO_3$ wetting cycle may be explained by the diminished mechanical coupling between the core and shell phases as the piezoelectric phase fraction is reduced.[23] However, the core–shell nanowires with the greatest $BaTiO_3$ fraction (*i.e.*, prepared with three $BaTiO_3$ wetting cycles) present an average ΔM_s of 2.87 ± 0.9%, which indicates the core and shell phases of the composite nanowires are strain coupled, potentially leading to magnetoelectric coupling.

To further examine the coupling between the core and shell phases, magnetization *vs.* temperature (M *vs.* T) measurements were performed using superconducting quantum interference device (SQUID) magnetometry. Core–shell nanowires prepared with three $BaTiO_3$ wetting cycles exhibit a distinct change in magnetization near the orthorhombic to rhombohedral phase transition for $BaTiO_3$, indicating the core and shell phases are strain coupled (Fig. S5, ESI†). Ultimately, the results presented from the VSM depolarization and SQUID *M vs. T* investigations provide indirect evidence for the presence of ME coupling, which is prominent with an increased fraction of $BaTiO_3$ in the core–shell nanowires.

As the thickness of the $BaTiO_3$ shell increases, it is anticipated that there will be a corresponding increase in the magnetic anisotropy of the $CoFe_2O_4$ core. To study this, a magnetic field was applied either parallel or perpendicular to the nanowire long axis while in template during VSM, corresponding to the magnetic easy and hard axes, respectively. The remnant magnetization for samples magnetized along the easy axis ($M_{r\parallel}$) *vs.* the hard axis ($M_{r\perp}$) was evaluated to probe the magnetic texture ($M_{r\parallel}/M_{r\perp}$) of the nanowires.[24] In Fig. 5a, $M_{r\parallel}/M_{r\perp}$ values are presented with respect to the nanowire length for $CoFe_2O_4$ (blue) and $CoFe_2O_4$–$BaTiO_3$ (orange) nanowires. The linear fit for the respective data sets is also presented as dashed lines to guide the eye. Fig. 5a reveals that the value for $M_{r\parallel}/M_{r\perp}$ increases with nanowire length. Interestingly, for $CoFe_2O_4$–$BaTiO_3$ nanowires, this effect is more prominent, which could be a result of increased anisotropy compared to that of $CoFe_2O_4$ nanowires due to the increasing aspect ratio of the $CoFe_2O_4$ core as the $BaTiO_3$ shell thickness increases. To investigate this effect further, the effective anisotropy constant was evaluated.

In Fig. 5b, the surface plot of the effective anisotropy constant (K_{eff}) as a function of nanowire length and $BaTiO_3$ yield during the nanowire synthesis is presented. The effect of shape anisotropy is clear, where K_{eff} increases as the nanowire length increases. Yet, K_{eff} also increases with $BaTiO_3$ yield, and presumably the $BaTiO_3$ shell thickness. There are two factors that could be influencing K_{eff}: (1) the increasing aspect ratio of the $CoFe_2O_4$ core due to increasing $BaTiO_3$ shell thickness or (2) decreased dipolar interactions between neighboring $CoFe_2O_4$ cores as the $BaTiO_3$ shell thickness increases. Ultimately, these results indicate that the anisotropy induced in the $CoFe_2O_4$ core can be tuned by how many $BaTiO_3$ wetting cycles are implemented during synthesis.

The K_{eff} of the nanowire arrays was calculated as the area between the magnetization curves taken along the easy and hard axes according to eqn (2).[25]

$$K_{eff} = \int_0^{M_s} H_{\perp} dM - \int_0^{M_s} H_{\parallel} dM \quad (2)$$

To clarify the origin of increasing anisotropy that was revealed in Fig. 5b, the contributions of K_{eff} are presented through a description of the effective anisotropy field (H_{eff}) of the $CoFe_2O_4$ core. H_{eff} can be evaluated for nanowire arrays with non-negligible magnetocrystalline anisotropy (as is the case for $CoFe_2O_4$) according to eqn (3).[26,27]

$$H_{eff} = 2\pi M_s - 6\pi M_s P + H_{mc} \quad (3)$$

with H_{eff} being related to K_{eff} according to eqn(4).[28]

$$H_{eff} = \frac{2K_{eff}}{\mu_o M_s} \quad (4)$$

where M_s is the saturation magnetization, P is the filling factor, H_{mc} is the contribution of the magnetocrystalline anisotropy, and μ_o is the vacuum permeability. The first two terms in eqn (3) are the magnetostatic and dipolar interaction contributions, respectively. In practice, a magnetic material will have a constant M_s and H_{mc}, and when deposited within a given AAO template, the value of P will also be constant. However, for $CoFe_2O_4$–$BaTiO_3$ core–shell nanowires, as the $BaTiO_3$ shell thickness increases, P will decrease and thus the dipolar interaction field will diminish and an increase in H_{eff} for $CoFe_2O_4$ will be observed. This explains why K_{eff} is modulated by both the nanowire length and the thickness of the $BaTiO_3$ shell, or more precisely, the spacing between $CoFe_2O_4$ cores while in template. This finding supports the notion that the processing conditions chosen can be used to tune the properties of core–shell ME nanowires.

In order to account for the variation in nanowire diameter in the presented analysis, the pore size distribution of the AAO templates was determined. The pore diameter (d_P) distribution will have direct implications on the magnitude of the filling factor, P, and ultimately, H_{eff}. Using ImageJ analysis, the magnitude of d_P was determined to be 199.6 ± 18.8 nm (Fig. S6, ESI†), (further details are presented within the ESI†). Due to the narrow size distribution of d_P, its impact on the analysis is expected to be negligible, with errors being relatively small (<10%). Therefore, minimal changes in the H_{eff} are expected.

In this communication a synthesis approach for core–shell ME nanowires, enabling tunability of the final composition in the nanocomposite, is presented. A range of sample compositions were investigated for $CoFe_2O_4$–$BaTiO_3$ nanowires. Notably, anisotropy in the $CoFe_2O_4$ core increases with $BaTiO_3$ shell thickness due to a combination of increased spacing between the $CoFe_2O_4$ cores and larger aspect ratios while in the template. Further exploration of sample composition is needed to establish a complete model of the effect of increasing shell thickness on the resulting anisotropy of the magnetic core and ME performance, this could be achieved using templates with varying spacing and pore diameters. Ultimately, this work shows great promise for the synthesis of ME nanowires with tunable anisotropy by a template-assisted process.

This work was supported in part by the National Science Foundation (NSF) I/UCRC on Multi-functional Integrated System Technology (MIST Center) IIP-1939009. This work was partly conducted at the Research Service Centers of the Herbert Wertheim College of Engineering at the University of Florida. The authors would like to thank Professors Julia Glaum and Juan Nino for their insightful discussion during the construction of the corona discharge poling station and Professor Carlos Rinaldi-Ramos and Eric Imhoff for assistance performing SQUID measurements.

Data availability

The data underlying this study are available in the published article and its ESI.†

Conflicts of interest

There are no conflicts to declare.

Notes and references

1 S. Manipatruni, D. E. Nikonov, C.-C. Lin, T. A. Gosavi, H. Liu, B. Prasad, Y.-L. Huang, E. Bonturim, R. Ramesh and I. A. Young, *Nature*, 2019, **565**, 35–42.
2 R. Ramesh and S. Manipatruni, *Proc. R. Soc. A.*, 2021, **477**, 20200942.
3 J. T. Heron, J. L. Bosse, Q. He, Y. Gao, M. Trassin, L. Ye, J. D. Clarkson, C. Wang, J. Liu, S. Salahuddin, D. C. Ralph, D. G. Schlom, J. Íñiguez, B. D. Huey and R. Ramesh, *Nature*, 2014, **516**, 370–373.
4 S. Manipatruni, D. E. Nikonov and I. A. Young, *Nat. Phys.*, 2018, **14**, 338–343.
5 S. Hohenberger, V. Lazenka, S. Selle, C. Patzig, K. Temst and M. Lorenz, *Phys. Status Solidi B*, 2020, **257**, 1900613.
6 Y. Liu, G. Sreenivasulu, P. Zhou, J. Fu, D. Filippov, W. Zhang, T. Zhou, T. Zhang, P. Shah, M. R. Page, G. Srinivasan, S. Berweger, T. M. Wallis and P. Kabos, *Sci. Rep.*, 2020, **10**, 20170.
7 M. J. Bauer, X. Wen, P. Tiwari, D. P. Arnold and J. S. Andrew, *Microsyst. Nanoeng.*, 2018, **4**, 37.
8 M. J. Bauer, A. Thomas, B. Isenberg, J. Varela, A. Faria and D. P. Arnold, *IEEE Sens. J.*, 2020, **20**, 7.
9 J. S. Andrew, J. D. Starr and M. A. K. Budi, *Scr. Mater.*, 2014, **74**, 38–43.
10 Y. Yan, Y. Zhou and S. Priya, *Appl. Phys. Lett.*, 2013, **102**, 052907.
11 J. L. Jones, J. D. Starr and J. S. Andrew, *Appl. Phys. Lett.*, 2014, **104**, 242901.
12 H. Chen, N. Wang, J. Di, Y. Zhao, Y. Song and L. Jiang, *Langmuir*, 2010, **26**, 11291–11296.
13 S. Xie, F. Ma, Y. Liu and J. Li, *Nanoscale*, 2011, **3**, 3152.
14 D. Sallagoity, C. Elissalde, J. Majimel, M. Maglione, V. A. Antohe, F. Abreu Araujo, P. M. Pereira de Sá, S. Basov and L. Piraux, *RSC Adv.*, 2016, **6**, 106716–106722.
15 S. Mushtaq, K. Shahzad, M. Rizwan, A. Ul-Hamid, B. H. Abbasi, W. Khalid, M. Atif, N. Ahmad, Z. Ali and R. Abbasi, *RSC Adv.*, 2022, **12**, 24958–24979.
16 Y. Zhang, B. Su, Y. Tian, Z. Yu, X. Wu, J. Ding, C. Wu, D. Wei, H. Yin, J. Sun and H. Fan, *Acta Biomater.*, 2023, **168**, 470–483.
17 D. Sallagoity, C. Elissalde, J. Majimel, R. Berthelot, U. C. Chung, N. Penin, M. Maglione, V. A. Antohe, G. Hamoir, F. Abreu Araujo and L. Piraux, *J. Mater. Chem. C*, 2015, **3**, 107–111.
18 L. R. Prado, N. S. De Resende, R. S. Silva, S. M. S. Egues and G. R. Salazar-Banda, *Chem. Eng. Process.*, 2016, **103**, 12–20.
19 U. A. Joshi, S. Yoon, S. Baik and J. S. Lee, *J. Phys. Chem. B*, 2006, **110**, 12249–12256.
20 T.-C. Huang, M.-T. Wang, H.-S. Sheu and W.-F. Hsieh, *J. Phys.: Condens. Matter*, 2007, **19**, 476212.
21 Y.-W. Ju, J.-H. Park, H.-R. Jung, S.-J. Cho and W.-J. Lee, *Mater. Sci. Eng., B*, 2008, **147**, 7–12.
22 D. Chien, A. N. Buditama, L. T. Schelhas, H. Y. Kang, S. Robbennolt, J. P. Chang and S. H. Tolbert, *Appl. Phys. Lett.*, 2016, **109**, 112904.
23 V. M. Petrov, J. Zhang, H. Qu, P. Zhou, T. Zhang and G. Srinivasan, *J. Phys. D: Appl. Phys.*, 2018, **51**, 284004.
24 C. S. Smith, R. Bowrothu, Y. Wang, F. Herrault, Y. K. Yoon and D. P. Arnold, *IEEE Trans. Magn.*, 2021, **57**, 1–5.
25 F. Li, T. Wang, L. Ren and J. Sun, *J. Phys.: Condens. Matter*, 2004, **16**, 8053–8060.
26 J. De La Torre Medina, M. Darques, L. Piraux and A. Encinas, *J. Appl. Phys.*, 2009, **105**, 023909.
27 V. Vega, T. Böhnert, S. Martens, M. Waleczek, J. M. Montero-Moreno, D. Görlitz, V. M. Prida and K. Nielsch, *Nanotechnology*, 2012, **23**, 465709.
28 B. D. Culity and C. D. Graham, *Introduction to Mangetic Materials*, IEEE, Hoboken, New Jersey, 2nd edn, 2009.

